

Approximating the end of nested sampling

Zixiao Hu, Artyom Baryshnikov, Will Handley

22 October 2023

ABSTRACT

This paper develops a technique to estimate the runtime of nested sampling which works for any nested sampling implementation. At each iteration, the dimensionality of the current set of samples is inferred, then used to extrapolate the known likelihood profile using a Gaussian model function, which allows the remaining evidence and prior volume at termination to be calculated. The method finds the right order of magnitude at all times, obtaining the true endpoint within standard error generally around the halfway point, and converges to the true value by the end of the run.

Key words: methods: data analysis – methods: statistical

1 INTRODUCTION

Nested sampling is a multi-purpose algorithm invented by John Skilling which simultaneously functions as a probabilistic sampler, integrator and optimiser (Skilling 2006). It was immediately adopted for cosmology, and is now used in a wide range of physical sciences including particle physics, materials science (Ashton et al. 2022) and machine learning (Higson et al. 2018). The core algorithm is unique in its estimation of volumes by *counting*, which makes high-dimensional integration feasible. It also avoids problems faced by traditional Bayesian algorithms, such as multi-modality.

The order of magnitude runtime of an algorithm, that is, whether termination is hours or weeks and months away, is of high importance to the end user. Currently, existing implementations of nested sampling (e.g. Feroz et al. 2009; Handley et al. 2015; Buchner 2021) either do not give an indication of runtime, or only provide crude measures of progress that do not directly correspond to the runtime.

This paper sets out a principled manner of endpoint estimation for nested sampling at each intermediate stage (as shown in Fig. 1), the key idea being to use the existing samples to predict the likelihood in the region we have yet to sample from. We begin with an overview of nested sampling in Section 2, followed by an examination of the anatomy of a nested sampling run to establish key concepts for endpoint prediction. Section 4 then outlines the methodology we use, including discussion and comparisons to previous attempts. Finally, Section 5 presents the results and discussions for toy and cosmological chains, before we conclude.

2 BACKGROUND

Let us begin with a brief description of the nested sampling algorithm to establish the necessary notation; for a more comprehensive treatment, we recommend Skilling’s paper and the textbook Sivia & Skilling (2006). For a given likelihood $\mathcal{L}(\theta)$ and prior $\pi(\theta)$, nested sampling simultaneously calculates the

```
Predicted endpoint: 25054 +/- 242
Progress: [=====>#####] 72%

-----
lives      | 500 |
phantoms   | 24310 |
posteriors | 18018 |
equals     | 245 |
-----
ncluster   = 1/1
ndeath     = 18018
nposterior = 18018
nequals    = 249
nlike      = 4159049
<nlike>     = 491.04 (9.82 per slice)
log(Z)     = -12.55 +/- 0.27
```

Figure 1. Output from POLYCHORD for a typical nested sampling run. The predicted endpoint, shown in red, is calculated using the method described in this paper.

Bayesian evidence

$$\mathcal{Z} = \int \mathcal{L}(\theta) \pi(\theta) \, d\theta \quad (1)$$

while producing samples of the posterior distribution

$$\mathcal{P}(\theta) = \frac{\mathcal{L}(\theta) \pi(\theta)}{\mathcal{Z}}. \quad (2)$$

The algorithm operates by maintaining a set of n_i *live points* sampled from the prior, which can vary in number throughout the run (Higson et al. 2019). At each iteration, the point with the lowest likelihood is removed and added to a list of *dead points*. A new point is then drawn from the prior, subject to the constraint that it must have a higher likelihood than the latest dead point. Repeating the procedure leads to the live points shrinking around peaks in the likelihood.

The integral in (1) is then evaluated by transformation to

a one-dimensional integral over the *prior volume* X

$$\mathcal{Z} = \int_0^1 \mathcal{L}(X) dX \approx \frac{1}{2} \sum_{i=1} \mathcal{L}(X_{i-1} - X_{i+1}), \quad (3)$$

where $X(\mathcal{L})$ is the fraction of the prior with a likelihood greater than \mathcal{L} . The prior volumes X_i are unknown, but can be statistically estimated as follows: one can define a *shrinkage factor* t_i at each iteration $X_i = t_i X_{i-1}$, such that

$$X_i = \prod_{k=1}^i t_k. \quad (4)$$

The t_i are the maximum of n_i points drawn from $[0, 1]$, so follow the distribution

$$P(t_i) = n_i t_i^{n_i-1} \quad (5)$$

$$\langle \log t_i \rangle = -\frac{1}{n_i}, \quad \text{Var}(\log t_i) = \frac{1}{n_i^2}. \quad (6)$$

The algorithm terminates when an user-specified condition is met; a popular choice is to terminate when the evidence in the live points falls below some fraction ϵ of the accumulated evidence e.g. 10^{-3} . The remaining live points are then killed off one by one without replacement and added to the evidence.

Uncertainties in the evidence are dominated by the spread in the prior volume distribution, and the simplest way to estimate them is by Monte Carlo sampling over sets of \mathbf{t} . For any given problem, the uncertainty in $\log \mathcal{Z}$ is proportional to $1/\sqrt{n_i}$, so n_i sets the resolution of the algorithm.

3 THE ANATOMY OF A NESTED SAMPLING RUN

The following section aims to make an inventory of the information available to us at an intermediate iteration i^* , which we shall eventually use to make endpoint predictions. We present an anatomy of the progression of a nested sampling run in terms of the prior volume compression, the log-likelihood increase, the inferred temperature, and the dimensionality of the samples.

3.1 Prior volume

The key feature of nested sampling is that the sampling is controlled by prior volume compression. The task is to find the posterior typically lying in a tiny fraction of the prior volume, a total compression which is quantified by the average information gain, or *Kullback-Leibler divergence*:

$$\mathcal{D}_{\text{KL}} = \int \mathcal{P}(\theta) \log \frac{\mathcal{P}(\theta)}{\pi(\theta)} d\theta. \quad (7)$$

The bulk of the posterior lies within a prior volume $X = e^{-\mathcal{D}_{\text{KL}}}$, which is the target compression. One gets there by iteratively taking steps of size $\Delta \log X_i = -1/n_i$, so that when we add up the contribution of each step in (6) we get

$$\text{E}(\log X_i) = -\sum_{k=1}^i \frac{1}{n_k}, \quad \text{Var}(\log X_i) = \sum_{k=1}^i \frac{1}{n_k^2}. \quad (8)$$

A constant step size in $\log X$ corresponds to a geometrically constant measure for the dead points (as shown in Fig. 2),

which is exactly needed to overcome the curse of dimensionality.

The same is not true for the live points, which are uniformly distributed in prior volume. As a result, the maximum live point is found at

$$\text{E}(\log X_{\text{min}}^{\text{live}}) = \text{E}(\log X_*) - \sum_{k=1}^{n_i} \frac{1}{n_k} \approx -\frac{i_*}{n_i} - \log n_i - \gamma, \quad (9)$$

with variance

$$\text{Var}(\log X_{\text{min}}^{\text{live}}) = \text{Var}(\log X_*) + \sum_{k=1}^{n_i} \frac{1}{n_k^2} \approx \frac{i_*^2}{n_i^2} + \frac{\pi^2}{6}, \quad (10)$$

where the large n_i limit is taken for the approximation to the harmonic series, γ being the Euler-Mascheroni constant.

The live points therefore only get us a factor of $\log n_i$ closer to the posterior bulk. In other words, it is not until we are around $\log n_i$ away from $\log X = -\mathcal{D}_{\text{KL}}$ that the samples look anything like the posterior. One can see from (7) that the divergence increases linearly with dimension, so for large dimensionalities and typical live point numbers $\lesssim 1000$, this does not happen until near the end of the run. Intuitively, it is because for a sharply peaked likelihood the live points are too diffuse to land there with any significant probability for most of the run.

The above results are summarised in Fig. 3

3.2 Log-likelihood

It is also useful to observe the distribution of the live and dead points in log-likelihood. We choose to examine a representative case of the d -dimensional multivariate Gaussian:

$$\log \mathcal{L} = \log \mathcal{L}_{\text{max}} - X^{2/d}/2\sigma^2 \quad (11)$$

with maximum point $\log \mathcal{L}_{\text{max}}$ and lengthscale σ to get an insight into the analytics. The likelihood monotonically increases towards $\log \mathcal{L}_{\text{max}}$, with the posterior samples eventually concentrated around the bulk at

$$\langle \log \mathcal{L} \rangle_{\mathcal{P}} = \log \mathcal{L}_{\text{max}} - \frac{d}{2}, \quad \text{Var}(\log \mathcal{L})_{\mathcal{P}} = \frac{d}{2}. \quad (12)$$

We can again find the size of each step in log-likelihood, as well as the expected location of the maximum live point. Let us define a likelihood normalised by the distance to the maximum:

$$y = \frac{\log \mathcal{L} - \log \mathcal{L}^*}{\log \mathcal{L}_{\text{max}} - \log \mathcal{L}^*}; \quad (13)$$

$y = 0$ corresponds to the current point $\log \mathcal{L}^*$ and $y = 1$ to the maximum $\log \mathcal{L}_{\text{max}}$. At each iteration, y increases by roughly

$$\lim_{n_i \rightarrow \infty} \Delta y \approx \frac{dy}{d \log X} \Delta \log X = \frac{2}{dn_i} \quad (14)$$

in the large n_i limit. We can again sum the harmonic series to see that the maximum live point is expected to be at

$$y_{(n_i)}^{\text{live}} = \frac{2 \log n_i}{d}, \quad (15)$$

where we have used the notation of order statistics to denote the $x_{(n)}$ as the maximum of n points. This is a very small fraction in high dimensions, showing again that until the end the live points are far from the posterior bulk, and certainly nowhere near the maximum.

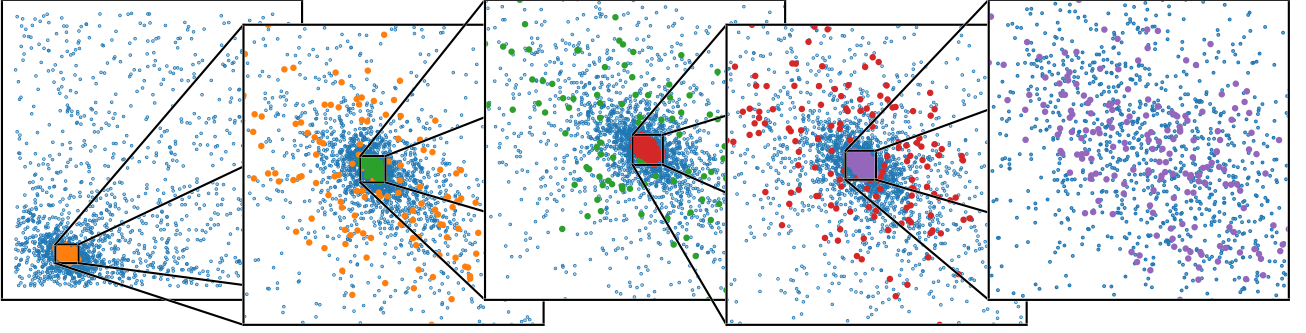


Figure 2. The dead points of a nested sampling run, recursively zoomed in. Their density is constant in $\log X$, which is a geometrically constant measure $\propto dV/V$, and hence scale invariant. The live points (larger dots) are uniform across the prior, plotted for comparison.

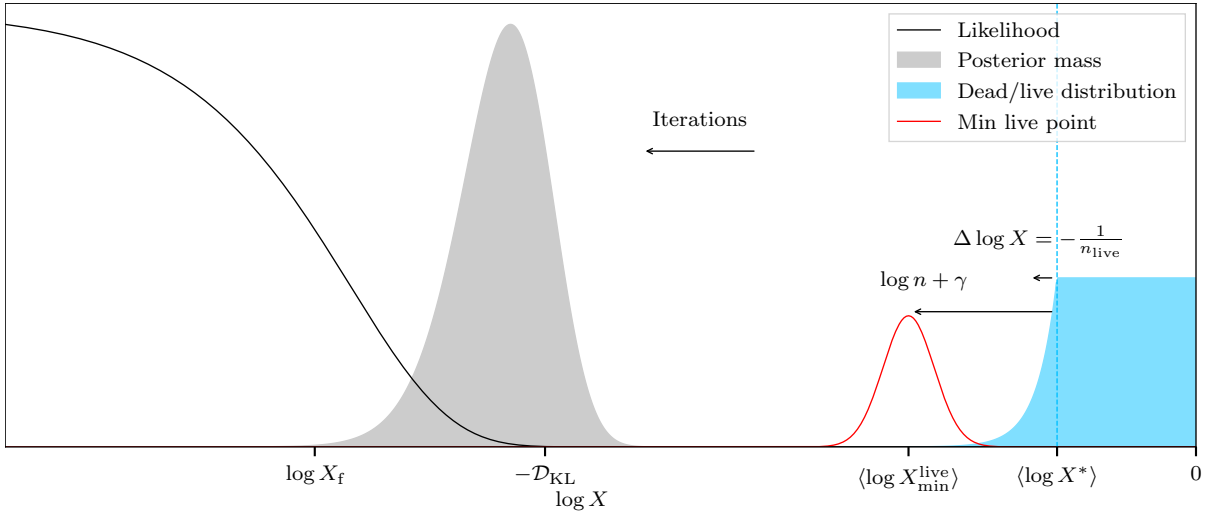


Figure 3. The distribution of the posterior mass in terms of $\log X$, the live points over the constrained prior and the smallest live point prior volume $\log X_{\min}^{\text{live}}$ at an intermediate iteration i_* . For large values of \mathcal{D}_{KL} i.e. informative posteriors and/or large dimensionalities, the maximum live point is very far from the posterior bulk until the very end of the run. Note that the x-axis in this plot is $\log X$, so that the run proceeds from right to left to emphasise that the enclosed prior volume iteratively gets smaller. Plots of the sort from here onwards will be in terms of $-\log X$, where the run will more naturally proceed from left to right.

The above also implies that the normalised distance between the highest and second highest live point is roughly

$$y_{(n_i)}^{\text{live}} - y_{(n_i-1)}^{\text{live}} \approx \frac{2}{d}. \quad (16)$$

Before reaching the posterior bulk, $\log \mathcal{L}_{\max} - \log \mathcal{L}^* > d/2$, so we must have

$$\log \mathcal{L}_{(n_i)}^{\text{live}} - \log \mathcal{L}_{(n_i-1)}^{\text{live}} > 1. \quad (17)$$

In other words, the highest likelihood point is always at least an order of magnitude greater than the second highest. It is therefore typically the case that nearly all of the posterior mass is concentrated in a single point, the maximum live point, until the very end of the run when the prior volumes have shrunk enough to compensate.

Aside: nested sampling as a maximiser

Previous literature (Akrami et al. 2010; Feroz et al. 2011) has explored the potential for nested sampling to be used as a

global maximiser, given its ability to handle multi-modalities. In particular, the latter authors emphasised that posterior samplers such as nested sampling find the bulk of the *mass*, not the maximum of the distribution, but that this can be remedied by tightening the termination criterion. We now use the machinery we have developed to put this statement in more quantitative terms.

A more rigorous derivation (Appendix A) shows that the maximum live point has mean and variance

$$\lim_{d, n_i \rightarrow \infty} y_{\max}^{\text{live}} \sim \frac{2 \log n_i}{d} \pm \sqrt{\frac{2}{3} \frac{\pi}{d}}. \quad (18)$$

Now let us take the dead point to be the termination point with likelihood $\log \mathcal{L}_{\text{end}}$ and prior volume X_{end} , so that

$$\epsilon = \frac{\int_0^{X_{\text{end}}} \mathcal{L} dX}{\int_0^\infty \mathcal{L} dX}. \quad (19)$$

Note that we have assumed that prior effects are negligible (so $1 = \infty$), and that $\epsilon \ll 1$ so that the denominator is approximately the accumulated evidence. Computing this for

(11), we find the answer in terms of lower incomplete gamma functions

$$\epsilon = 1 - \frac{\Gamma_{d/2} \left(X_{\text{end}}^{2/d} / 2\sigma^2 \right)}{\Gamma(d/2)}. \quad (20)$$

Taking the $X_{\text{end}} \ll (\sqrt{2}\sigma)^d$ limit (almost certainly valid at termination) we find

$$\lim_{X_{\text{end}} \ll (\sqrt{2}\sigma)^d} \epsilon \approx \frac{X_{\text{end}}}{(\sqrt{2}\sigma)^d \Gamma(1 + \frac{d}{2})} = \frac{(\log \mathcal{L}_{\text{max}} - \log \mathcal{L}_{\text{end}})^{\frac{d}{2}}}{\Gamma(1 + \frac{d}{2})}. \quad (21)$$

We thus have an expression relating \mathcal{L}_{end} at termination to the termination fraction ϵ . This becomes yet more pleasing in the large d limit, since $\epsilon^{2/d} \rightarrow 1$, we find via a Stirling approximation:

$$\lim_{d \rightarrow \infty} \log \mathcal{L}_{\text{end}} \approx \log \mathcal{L}_{\text{max}} - \frac{d}{2e}. \quad (22)$$

In the event that we keep ϵ in, we replace $\frac{d}{2e} \rightarrow \frac{d}{2e} \epsilon^{2/d}$, so we can of course battle the $\frac{d}{2e}$ term, but this becomes exponentially difficult in high dimensions.

Putting this together, taking \mathcal{L}_* in (13) to be \mathcal{L}_{end} , and combining this with (18) we find

$$\log \mathcal{L}_{\text{max}}^{\text{live}} \approx \log \mathcal{L}_{\text{max}} - \frac{d}{2e} + \frac{\log n}{e} \pm \frac{\pi}{\sqrt{6e}}, \quad (23)$$

showing that in general nested sampling will finish at a contour $d/2e$ away from the maximum log-likelihood. The final set of n live points gets you $\log n/2e$ closer, with a chance of getting $\sim \pi/\sqrt{6e} = 0.472$ closer still by statistical fluctuation.

A plot of the log-likelihood distribution at the end of a run is shown in Fig. 4

3.3 Temperature

Motivations

As shown in the previous section, midway through the run nearly all of the posterior mass is concentrated at a single point. However, this does not capture the *structure* of the posterior that has been explored and all of the information it provides.

We have the potential to fix this because nested sampling is invariant to monotonic transformations, so we can transform the likelihood as $\mathcal{L} \rightarrow \mathcal{L}^\beta$ without loss of information by trivially reweighting the samples. Increasing β worsens the situation, while $\beta \rightarrow 0$ simply gives back the prior. There is, however, a significant intermediate range which makes the samples look like a posterior centred at the present contour, which will allow us to recover the structure of the samples. A schematic of the procedure is shown in Fig. 5.

At this point it is relevant to note the correspondence between Bayesian inference and statistical mechanics, from which the above transform is derived. If one equates the parameters to microstates i , the negative log-likelihood to the microstate energy E_i , and the prior to the density of states g_i , then the posterior as given by the generalised Bayes' rule is the canonical ensemble

$$p(E_i) = \frac{g_i e^{-\beta E_i}}{\mathcal{Z}(\beta)} \leftrightarrow \mathcal{P}_\beta(\theta) = \frac{\mathcal{L}^\beta(\theta) \pi(\theta)}{\mathcal{Z}(\beta)} \quad (24)$$

at the inverse temperature $\beta = 1/T$. As noted by [Habeck](#)

(2015), thermal algorithms such as thermodynamic integration ([Gelman & Meng 1998](#)) get the evidence by evolving through a series of canonical ensembles via some temperature schedule, but nested sampling instead maintains *microcanonical* ensembles, which are the iso-likelihood contours. Each step moves at constant relative volume entropy $\Delta \log X$, which allows the algorithm to handle phase transitions ([Páray et al. 2010](#)).

Because the temperature of a microcanonical ensemble is a derived property rather than a parameter, there is some freedom in its definition. Returning to our original motivation, we make the connection that the temperature is the reweighting $\mathcal{L} \rightarrow \mathcal{L}^\beta$ which centers the ensemble around the current energy. We now present several temperatures that achieve this aim, each of which one can plausibly consider to be the current temperature of a nested sampling run.

A. Microcanonical temperature

The obvious candidate is the microcanonical temperature $\partial S / \partial E$, where the volume entropy is $\log X$ and the energy is as usual $-\log \mathcal{L}$. This gives the density of states; as discussed in Skilling's original paper,

$$\beta_M = - \left. \frac{d \log X}{d \log \mathcal{L}} \right|_{\log \mathcal{L}^*}. \quad (25)$$

is the β at which $\mathcal{L}^\beta X$ peaks at $\log X^*$, if we assume differentiability, which is exactly the intuition we were aiming for to put the ensemble bulk at the current contour. Its value can be easily obtained via finite difference of the $\log \mathcal{L}$ and $\log X$ intervals, albeit subject to an arbitrary window size for the differencing (in practice, we find that above a threshold of around 10 iterations the result is fairly insensitive to this choice).

The ensemble bulk can be placed at the current point in several other plausible ways, which are discussed below.

B. Canonical temperature

Another temperature considered by Habeck is that at which the current energy (i.e. $-\log \mathcal{L}^*$) is the average energy of the entire ensemble. One can obtain it by inverting

$$\langle \log \mathcal{L} \rangle_{\mathcal{P}_\beta} = \log \mathcal{L}^* \quad (26)$$

to get the 'canonical' temperature β_C . While β_M is derived from (the gradient of) a single contour, this temperature uses the entire ensemble. It has the desirable property that it rises monotonically with compression, in analogy to a monotonic annealing schedule.

C. Bayesian temperature

We furthermore propose a temperature β_B that is obtained via Bayesian inference, which returns a distribution rather than a point estimate. Since each value of β leads to a different likelihood \mathcal{L}^β , one can consider the posterior distribution as a function of $\log X$ to be *conditioned* on β . We can therefore write

$$\mathcal{P}(\log X | \beta) = \frac{\mathcal{L}^\beta(X) X}{\mathcal{Z}(\beta)}. \quad (27)$$

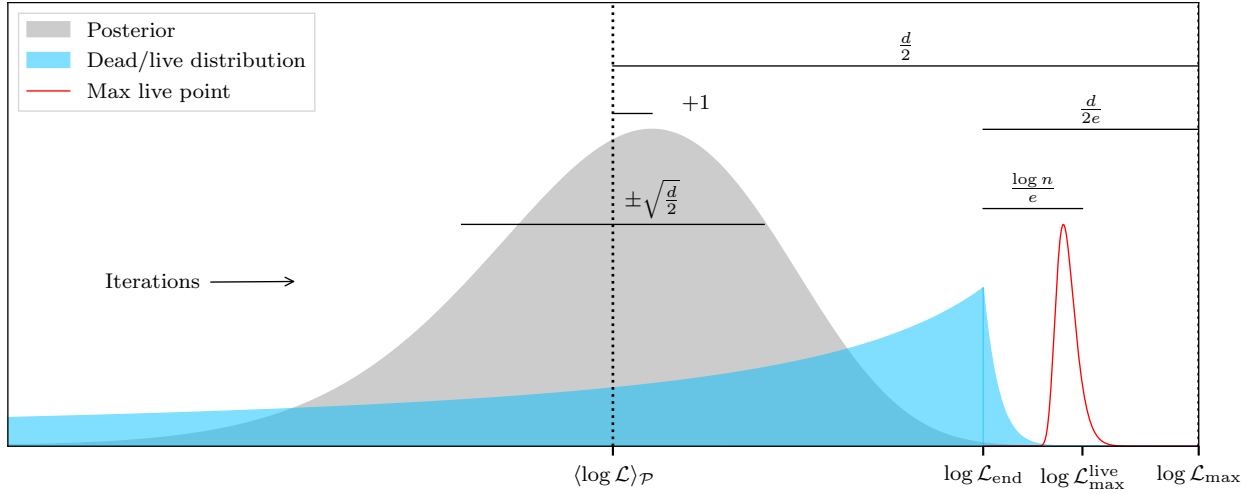


Figure 4. Distribution of samples as a function of $\log \mathcal{L}$, showing the posterior $\mathcal{P}(\log \mathcal{L})$, the distribution of the live points $\pi(\log \mathcal{L} | \mathcal{L} > \mathcal{L}_*)$, and the distribution of the maximum likelihood live point $P(\log \mathcal{L}_{\max}^{\text{live}})$. The distances are shown between these locations at the end of the run, the key takeaway being that in high dimensions the highest log-likelihood point of a nested sampling run is nowhere near the maximum in high dimensions.

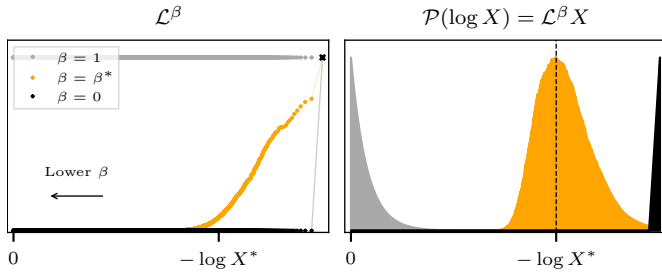


Figure 5. The likelihood and posterior as a function of $\log X$ in the middle of a nested sampling run. Almost all of the posterior mass is concentrated at a single point with the highest compression, because it is orders of magnitude higher in likelihood. Reducing β reweights to shift the posterior mass; taking $\beta \rightarrow 0$ goes too far and gives back the prior, but there is some intermediate $\beta = \beta^*$ which is significant because it centres the posterior at the current contour.

What we would really like is the distribution of β at the present iteration, so the natural step is to invert this via Bayes' rule;

$$P(\beta | \log X^*) = \frac{\mathcal{P}(\log X^* | \beta) P(\beta)}{P(\log X)}. \quad (28)$$

As with all Bayesian analyses, the distribution of β is fixed up to a prior, which we choose to be uniform in β . The obtained temperatures are consistent with the previous two choices, which may seem oddly coincidental. However, closer inspection reveals that large values of $P(\beta | \log X^*)$ are the temperatures with a large value of the posterior at the present contour, normalised by the corresponding evidence. Thus the Bayesian temperature uses the same idea as the microcanonical one, except it accounts for the spread in the result.

Comparisons

Fig. 6 shows the three temperatures as a function of compression for two cases, one containing a phase transition and

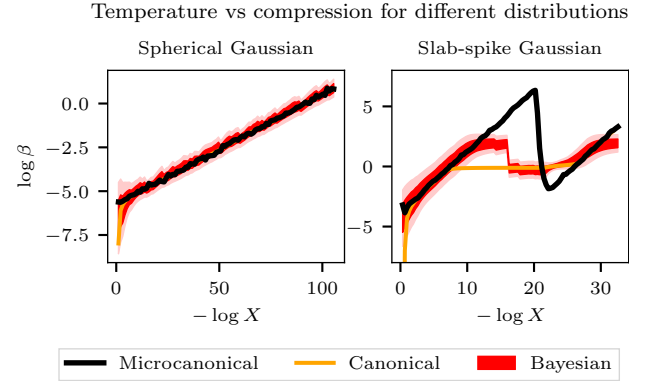


Figure 6. Inferred temperatures using the microcanonical, canonical and Bayesian definitions. All are consistent for a single phase, but differ during a phase transition.

one without. They are consistent in both cases when there is a single dominant phase, but differ during a phase transition. The canonical temperature is the only one that rises monotonically with compression.

One should keep in mind that despite the above theoretical reasoning, our introduction of the likelihood transformation was ultimately motivated by our wish to utilise the extra degree of freedom it provides. As we will see below, we recommend choosing the exact definition depending on what is useful for the transformation to do.

3.4 Dimensionality

We can immediately use the inferred temperature to track how the effective dimensionality of the posterior changes throughout the run, which was previously inaccessible. Handley & Lemos (2019) demonstrated that at the end of a run, a measure of the number of constrained parameters is given by the Bayesian model dimensionality (BMD), defined as the

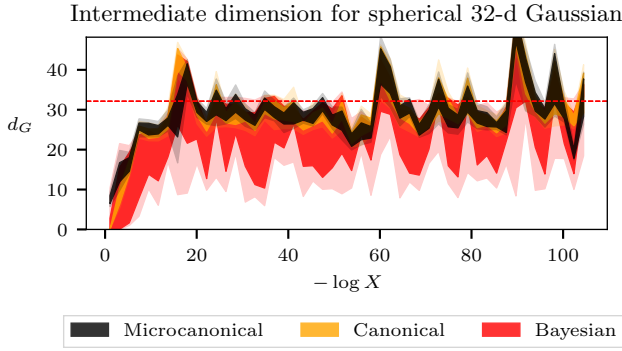


Figure 7. Dimensionality estimates using the different temperatures for a spherical 32-d Gaussian. Again, all are consistent, but the Bayesian definition has an uncertainty which includes the true value far more consistently than for the other definitions.

posterior variance of the information content:

$$\frac{d_G}{2} = \int \mathcal{P}(\theta) \left(\log \frac{\mathcal{P}(\theta)}{\pi(\theta)} - \mathcal{D}_{\text{KL}} \right)^2 d\theta = \langle \mathcal{I}^2 \rangle_{\mathcal{P}} - \langle \mathcal{I} \rangle_{\mathcal{P}}^2. \quad (29)$$

Calculating the quantity using intermediate set of weighted samples (which is concentrated at a single point) leads to vanishing variance, hence also dimensionality. However, we can recover the structure of the posterior together with the true dimensionality by adjusting the temperature. Dimensionality estimates are plotted in Fig. 7 for a spherical 32-d Gaussian, for which the true dimensionality is known.

The different choices of temperature are again consistent, but for the rest of this paper we choose the Bayesian β , because it provides a better reflection of the uncertainty in the estimate; the others, while fluctuating around the true value, are often many standard errors away from the true value at each single point.

Anisotropic compression

Plots of samples dimensionality against compression also draw attention to the *directions* in which the samples are constrained throughout the run. As a concrete example, consider an elongated Gaussian in a unit hypercube prior with $\mu = \mathbf{0}$ and $\Sigma = \text{diag}(10^{-3}, 10^{-3}, 10^{-3}, 10^{-6}, 10^{-6}, 10^{-6})$, for which the dimensionality estimates are plotted in Fig. 8. Alongside is a view of the distribution of live points across the prior for two directions with different scales, which shows the level to which those parameters have been constrained at different times.

A feature of nested sampling made apparent here is that parameters with high variance are initially ‘hidden’. Compression occurs in the direction which is most likely to have a sample of higher likelihood, and initially it is much easier to find a better point along the direction of a parameter that is poorly constrained. Lower variance parameters are constrained much later, and before that happens it appears as though those parameters have a uniform distribution.

It is important to appreciate that at lower compressions the samples truly lie in a lower-dimensional space, rather than some artefact of the way we view them. Anticipating the full dimensionality of the space is therefore just as impossible as that associated with a slab-spike geometry, so in this sense such geometries contain a ‘compressive phase transition’.

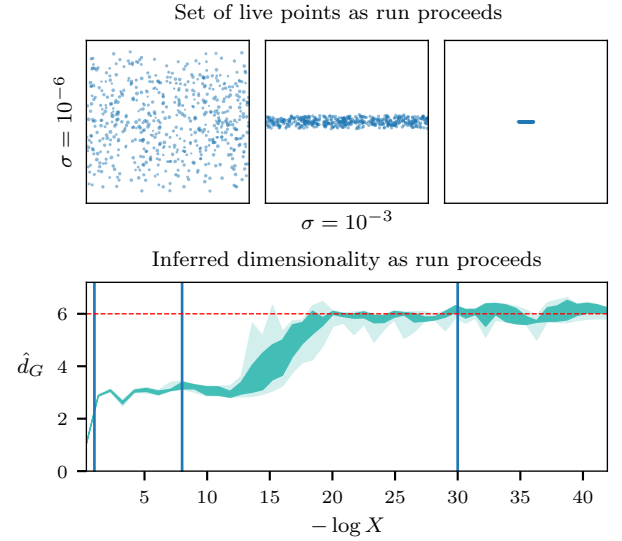


Figure 8. Dimensionality estimates for a Gaussian that is elongated in half of its dimensions. The locations of the live points in the prior are shown at three stages, indicated by the vertical lines. As can be seen from the live point distribution, the prior does not compress in the higher variance direction until much later in the run, and early on it appears as if those directions are completely unconstrained.

4 ENDPOINT PREDICTION

The time complexity of nested sampling (Petrosyan & Handley 2022) is

$$T \propto n_i \times \langle \mathcal{T}\{\mathcal{L}(\theta)\} \rangle \times \langle f_{\text{sampler}} \rangle \times \mathcal{D}_{\text{KL}}. \quad (30)$$

The second term is the relatively constant time per likelihood evaluation. The third is the average number of evaluations required to replace a dead point with a live point at higher likelihood, which is given by the implementation and usually does not vary in orders of magnitude. The primary unknown during a run, and therefore our primary interest, is the final term: the compression required to get from prior to posterior.

Further exploration can be found in the talk [9] and the upcoming paper Handley (2023b).

4.1 The termination prior volume

To be exact, one wishes to find the compression factor $\log X_f$ at which the termination criterion is met, which is larger in magnitude than \mathcal{D}_{KL} (Fig. 3). The problem is that at an intermediate iteration we only know the posterior up to the maximum log-likelihood live point, which until just before the end is quite far from the posterior bulk.

In order to get an idea of where the true posterior bulk sits, we need to predict what the posterior looks like past the highest live point. We do this by *extrapolating* the known likelihood profile; that is, the trajectory of $\mathcal{L}(X)$ traced out by the live and dead points.

One would never use this predicted posterior to do inference, since more accuracy can always be achieved by simply finishing the run. However, it is more than sufficient for making a prediction for $\log X_f$. Quantitatively, this proceeds as follows: fit a function $f(X, \phi)$ with some parameters ϕ to the

known likelihood profile, which allows us to express the prior volume we need to compress to as

$$\Delta \mathcal{Z} = \epsilon \mathcal{Z}_{\text{tot}}, \quad (31)$$

$$\int_0^{X_f} f(X, \phi) dX = \epsilon \left(\int_0^{X_i} f(X, \phi) dX + \mathcal{Z}_{\text{dead}} \right), \quad (32)$$

where X_i is the volume of the iteration we have currently compressed to, and $\mathcal{Z}_{\text{dead}}$ is the evidence we have accumulated up to this point. X_f can then be identified by solving the above equation either analytically or numerically.

Once X_f is known, the corresponding iteration count depends on the live point schedule. The conversion is easiest in the constant n_i case; at each iteration $\log X$ decreases by $1/n$, so the total number of iterations N_f will be

$$N_f = -n \log X_f. \quad (33)$$

4.2 How to extrapolate?

A key observation is that the Bayesian model dimensionality is the equivalent dimension of the posterior if it were actually Gaussian. Fitting a Gaussian of this dimension to the likelihood profile therefore makes a reasonable approximation to the true distribution, without explicitly assuming the form of the likelihood function. The parameterisation of the Gaussian that we fit is the same as that given in Section 3.2, which we shall repeat here for clarity;

$$f(X; \phi) = \log \mathcal{L}_{\text{max}} - X^{2/d}/2\sigma^2 \quad (34)$$

The extrapolation then proceeds thus:

- (i) Find the current dimensionality d_G^* of the posterior at the Bayesian temperature
- (ii) Take the live point profile and do a least squares fit to (34), stipulating that $d = d_G^*$ to infer $\log \mathcal{L}_{\text{max}}$ and σ
- (iii) Use the likelihood predicted by these parameters to solve (32) for X_f

The advantage of fitting a Gaussian is that the procedure can be sped up analytically. Firstly, the least squares regression is trivial because analytic estimators exist; the cost function

$$C^2(\log \mathcal{L}_{\text{max}}, \sigma) = \sum_i |\log \mathcal{L}_i - f(X_i; \log \mathcal{L}_{\text{max}}, \sigma)|^2 \quad (35)$$

is minimised with respect to $(\log \mathcal{L}_{\text{max}}, \sigma)$ when

$$\sigma^2 = \frac{N \sum_i X_i^{4/d} - \left(\sum_i X_i^{2/d} \right)^2}{2 \sum_i \log \mathcal{L}_i \sum_i X_i^{2/d} - 2N \sum_i X_i^{2/d} \log \mathcal{L}_i}, \quad (36)$$

and

$$\log \mathcal{L}_{\text{max}} = \frac{1}{N} \sum_i \log \mathcal{L}_i + \frac{1}{2N\sigma^2} \sum_i X_i^{2/d}. \quad (37)$$

Secondly, the termination prior volume can also be obtained analytically. Rewriting Eq. (32) in terms of the Gaussian parameters gives

$$\epsilon = \frac{\int_0^{X_f} \mathcal{L}_{\text{max}} \exp(-X^{2/d}/2\sigma^2) dX}{\int_0^{X_i} \mathcal{L}_{\text{max}} \exp(-X^{2/d}/2\sigma^2) dX + \mathcal{Z}_{\text{dead}}}. \quad (38)$$

The integrals have the analytic solution

$$\int_0^{X_k} \mathcal{L}_{\text{max}} \exp(-X^{2/d}/2\sigma^2) dX = \frac{d}{2} \cdot (\sqrt{2}\sigma)^d \cdot \gamma_k \quad (39)$$

where $\gamma_k = \Gamma_{d/2}(X_k^{2/d}/2\sigma^2)$ is the lower incomplete gamma function. After taking the inverse of γ and a few more steps of algebra, we arrive at

$$\log X_f = \frac{d}{2} \log 2\sigma^2 + \log \Gamma_{d/2}^{-1} \left(\epsilon \gamma_i + \frac{\epsilon \mathcal{Z}_{\text{dead}}}{(2\sigma^2)^{d/2} \mathcal{L}_{\text{max}}} \right), \quad (40)$$

and N_f is of course just $-n_i$ multiplied by this. Intuitively, the above procedure can be thought of as inferring the number of constrained parameters, then extrapolating them up to find the point at which they will be fully constrained.

One might wonder why we do not obtain d via least squares regression together with the other parameters; extensive testing has shown it to be far less stable.

4.3 Alternative approaches

We consider here several alternative approaches to endpoint estimation to compare against our method.

A. Integral progress

One alternative approach, used in ULTRANEST (Buchner 2021), derives a progress bar based on the fraction of the accumulated integral compared to the remaining integral, approximated as

$$\mathcal{Z}_{\text{rem}} \approx \mathcal{L}_{\text{max}}^{\text{live}} X^*. \quad (41)$$

There are a few problems here. Firstly, runtime is proportional to compression rather than accumulation of the integral, since it takes just as long to traverse the width of the bulk as it does any other width. Secondly, because of the point-like nature of the posterior mid-run, the remaining integral approximated as such holds nearly all of the evidence, so the relative fraction of the accumulated and remaining evidence is simply be zero for most of the run. Furthermore, approximation (41) is always an underestimate, because as previously found the maximum live point is generally nowhere near the true maximum.

This approach can be useful in low dimensions when the live points are always near the maximum, but in general is less reliable.

B. Extrapolating evidence increments

Seasoned users of nested sampling might be curious how the method compares to simply extrapolating the increments of evidence to roughly estimate when the evidence converges. We do this for a spherical Gaussian and compare it to our method. At an intermediate stage of the run, the most recent outputs might look something like that shown in the first two columns of the table in Fig. 9. Extrapolating those data to a linear and exponential profile yields endpoint estimates plotted in the graph to the right.

The linear extrapolation is clearly an underestimate, since it fails to account for the long tail of the nonlinear profile. The increments are also not quite exponential, since the exponential fit leads to a large overprediction. The predicted endpoint over the course of a run for $d = 16$, $\sigma = 0.01$, as shown in Fig. 10, shows the same result. One might expect an average to be more accurate, but this tends to be biased

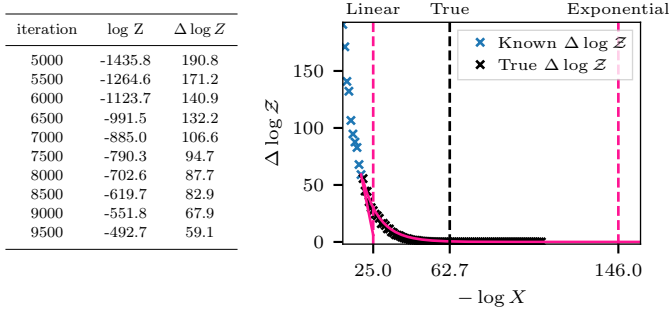


Figure 9. Extrapolating the increments of evidence. The left column shows the output of a nested sampling run, and the right column shows the extrapolation.

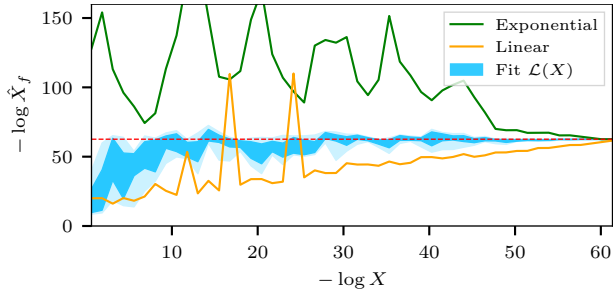


Figure 10. Endpoint predictions for a spherical Gaussian. Extrapolating the evidence increments in a linear/exponential manner under/overpredicts the endpoint, both of which do considerably worse than the method of extrapolating the likelihood.

towards the exponential prediction, and there is no obvious choice of weighting that would fix this.

More importantly, we find that for real likelihoods which have an element of noise the extrapolation often diverges, for instance when the increments do not monotonically decrease. Directly extrapolating the evidence increments is therefore far less stable than the previous method, and generally not a reliable method for prediction.

5 RESULTS

Now that we have a method for predicting the endpoint, it can be tested on a range of distributions. We begin by considering a series of toy examples to explore the capabilities and limitations of the method, before presenting results for real cosmological chains.

5.1 Toy examples

A. Gaussians

Predictions for spherical Gaussians of various dimensions are shown in Fig. 11 as a benchmark for when fitting a Gaussian distribution is exact. All were run with $n_i = 500$ except for one $n_i = 2000$ for comparison, with each Gaussian having a width of $\sigma = 0.01$. The correct endpoint is recovered to within standard error at all points except the very beginning, when the parameters have hardly been constrained.

We note that as with nested sampling in general, increasing n_i improves the resolution and reliability of the inferences,

which can be seen from the middle two plots. We also observe the effect of elongating the Gaussian, using the same example as Section 3.4. Fig. 12 shows a step-like trend similar to the inferred dimensionalities, reflecting the fact that the full dimensionality is undetectable at lower compression factors. The endpoint for a likelihood whose remaining three directions are completely unconstrained coincides with our predictions at early iterations, showing that the two cases are indistinguishable.

B. Cauchy

One case that might be expected to cause problems is the pathological Cauchy distribution, which is far from a Gaussian. Fig. 13 shows the predictions for a likelihood of the form

$$\log \mathcal{L} = \log \mathcal{L}_{\max} - \frac{1+d}{2} \log \left(1 + \frac{X^2}{\gamma^2} \right), \quad (42)$$

choosing $d = 10$ and allowing γ to vary. The correct estimate is obtained to within standard error by about halfway, but before that is quite off. The key limitation is that the estimate is wrong early on not because the compression is anisotropic, or that there is a phase transition; rather, it is a limitation of the reducing the likelihood to a Gaussian via the BMD, which is itself less stable for a Cauchy.

However, the right order of magnitude is obtained at all times, so this is not a major concern. The Cauchy is also a pathological case, and the same problem does not rear its head in more realistic cases, as we shall see next.

5.2 Cosmological examples

Finally, we evaluate the method on real cosmological chains. Fig. 14 presents the endpoints (calculated after the fact) for nested sampling runs for curvature quantification on several common cosmological datasets (details in Handley (2021)).

The SH0ES, BAO and LENSING chains are ‘easy’ low \mathcal{D}_{KL} inferences, so it is expected that the correct endpoint is inferred practically from the start. The PLANCK endpoints, on the other hand, are not correct until at least midway through. However, this is expected from the covariance of the PLANCK likelihood, which consists of principal components of many scales and therefore elongated in many dimensions. It is therefore of the same class as the elongated Gaussian presented in Section 3.4; the samples exist in a lower dimensional subspace mid-run, which slowly increases to the full dimensionality only at the end of the run.

6 CONCLUSION

We have presented a method for predicting the endpoint of a nested sampling run, by inferring the Bayesian model dimensionality of a set of samples mid-run and using it to extrapolate the known likelihood profile.

The method in general converges to the correct endpoint by about the halfway point, and gets the correct order of magnitude throughout. Consistent predictions are obtained for both toy and cosmological examples. The accuracy is typically limited by the information available mid-run, either because of a phase transition or because the anisotropy of the nested sampling compression. Pathological distributions,

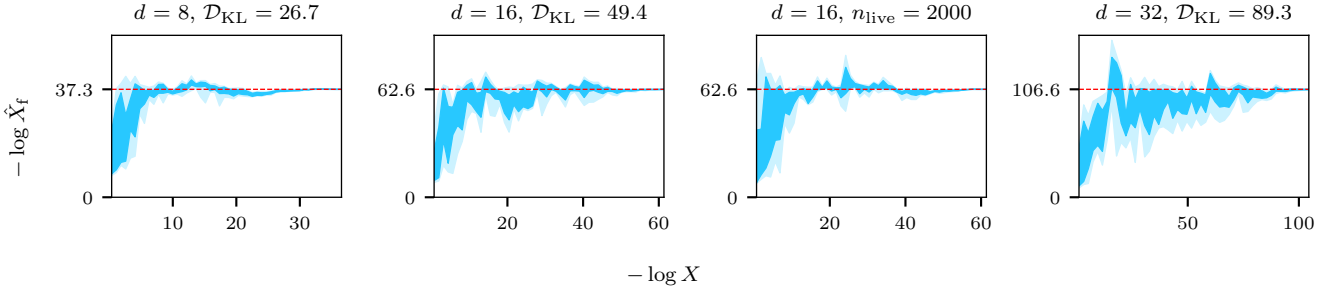


Figure 11. Endpoint predictions for a spherical Gaussian run with $n_i = 500$ (except for the third plot from left). The correct endpoint is obtained for all but the earliest iterations, and the uncertainty is controlled by the number of live points, which can be seen from the two $d = 16$ plots.

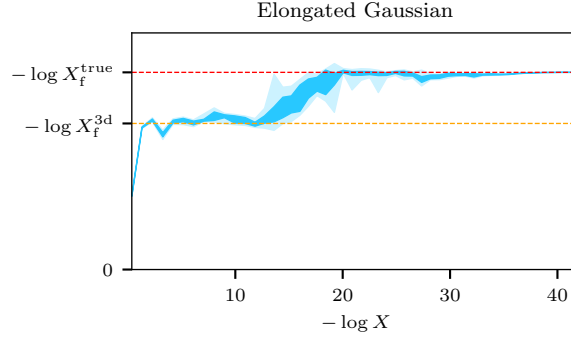


Figure 12. Endpoint prediction for an elongated Gaussian. At early stages, the full dimensionality is undetectable, and the endpoint is predicted to be the same as for a likelihood with three unconstrained directions. Only once the prior has been compressed enough to constrain the other three directions does the prediction converge to the true value.

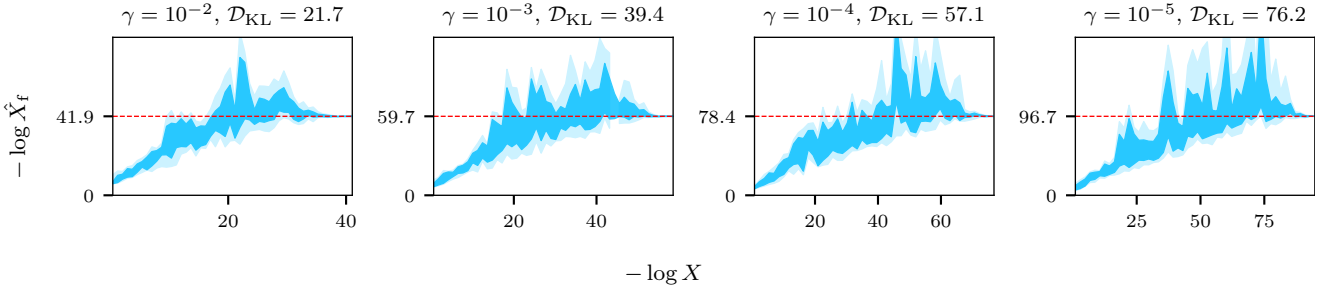


Figure 13. Predictions for the Cauchy distribution for various widths γ and $n_i = 500$. The endpoint is underestimated for the first half of the run, but this is a limitation of the Gaussian approximation rather than a lack of information mid-run.

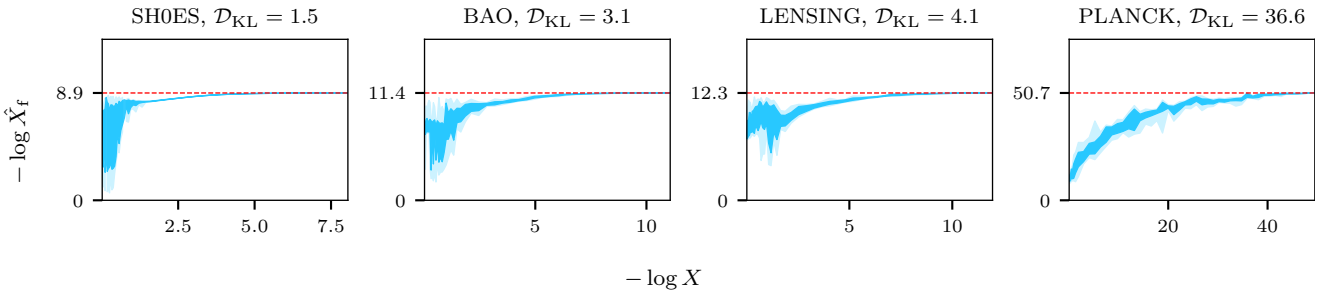


Figure 14. Endpoint predictions for cosmological likelihoods. The first three low \mathcal{D}_{KL} inferences get the correct endpoint from the start, while the PLANCK chain takes longer to converge because the likelihood is highly covariant and thus subject to anisotropic compression, which makes the samples lie in a lower dimensional subspace mid-run.

such as a Cauchy, lead to less stable inferences of the dimensionality and expose the limitations of a Gaussian approximation, though the order of magnitude is still correct.

Further work can be done to experiment with more flexible basis functions for regression of the likelihood profile, so that it is less dependent on the Gaussian approximation.

APPENDIX A: THE MAXIMUM LIVE LOG-LIKELIHOOD

Assume a Gaussian likelihood

$$\log \mathcal{L} = \log \mathcal{L}_{\max} - X^{2/d}/2\sigma^2. \quad (\text{A1})$$

The distribution of the true posterior in $\log \mathcal{L}$ is

$$P(\log \mathcal{L}) = \frac{1}{\Gamma(\frac{d}{2})} e^{\log \mathcal{L} - \log \mathcal{L}_{\max}} (\log \mathcal{L}_{\max} - \log \mathcal{L})^{\frac{d}{2}-1} \quad (\text{A2})$$

i.e. $2(\log \mathcal{L}_{\max} - \log \mathcal{L}) \sim \chi_d^2$. The posterior average and variance of $\log \mathcal{L}$ are given by

$$\langle \log \mathcal{L} \rangle_{\mathcal{P}} = \log \mathcal{L}_{\max} - \frac{d}{2}, \quad \text{Var}(\log \mathcal{L})_{\mathcal{P}} = \frac{d}{2}. \quad (\text{A3})$$

Meanwhile, the live points are uniformly distributed over the constrained prior and hence have probability distribution

$$P(\log \mathcal{L}) = \frac{d}{2} \frac{(\log \mathcal{L}_{\max} - \log \mathcal{L})^{\frac{d}{2}-1}}{(\log \mathcal{L}_{\max} - \log \mathcal{L}_*)^{\frac{d}{2}}} [\log \mathcal{L}_* < \log \mathcal{L} < \log \mathcal{L}_{\max}], \quad (\text{A4})$$

It is helpful at this stage to define a parameter

$$y = \frac{\log \mathcal{L} - \log \mathcal{L}_*}{\log \mathcal{L}_{\max} - \log \mathcal{L}_*} \quad (\text{A5})$$

as a normalised measure of how far a point is between the latest dead point and the maximum log-likelihood, with $y = 0$ corresponding to \mathcal{L}_* and $y = 1$ to \mathcal{L}_{\max} , so that

$$P(y) = \frac{d}{2} (1-y)^{\frac{d}{2}-1} \quad [0 < y < 1]. \quad (\text{A6})$$

We now seek the distribution for the maximum likelihood of the live points, $\log \mathcal{L}_{\max}^{\text{live}}$. Using the result that the maximum of n variables with cumulative distribution $F(y)$ follows $\frac{d}{dy}(1 - (1 - F(y))^n)$, we obtain

$$P(y_{\max}^{\text{live}}) = \frac{nd}{2} (1 - y_{\max}^{\text{live}})^{\frac{d}{2}-1} \left(1 - (1 - y_{\max}^{\text{live}})^{\frac{d}{2}}\right)^{n-1} \quad [0 < y_{\max}^{\text{live}} < 1], \quad (\text{A7})$$

which may be roughly summarised as

$$y_{\max}^{\text{live}} \sim 1 - \frac{\Gamma(1 + \frac{2}{d})\Gamma(1+n)}{\Gamma(1 + \frac{2}{d} + n)} \pm \left(\frac{\Gamma(1+n)\Gamma(1 + \frac{4}{d})}{\Gamma(1 + \frac{4}{d} + n)} - \frac{\Gamma(1 + \frac{2}{d})^2\Gamma(1+n)^2}{\Gamma(1 + \frac{2}{d} + n)^2} \right)^{\frac{1}{2}}, \quad (\text{A8})$$

or in the large d, n limit

$$\lim_{d \rightarrow \infty} y_{\max}^{\text{live}} \sim \frac{2H_n}{d} \pm \left(\frac{2(\pi^2 - 6\Psi^{(1)}(1+n))}{3d^2} \right)^{\frac{1}{2}}, \quad (\text{A9})$$

$$\lim_{d, n \rightarrow \infty} y_{\max}^{\text{live}} \sim \frac{2 \log n}{d} \pm \sqrt{\frac{2}{3}} \frac{\pi}{d}, \quad (\text{A10})$$

where $\psi^{(1)}$ is the trigamma function and H_n is the n th harmonic number.

This shows that in general the live points are nowhere near the maximum log-likelihood at any iteration, though they do steadily squeeze the interval $[\log \mathcal{L}_*, \log \mathcal{L}_{\max}]$. In particular, in high dimensions n only gets us harmonically/logarithmically closer, whilst d pushes us linearly further away.

REFERENCES

- Akrami Y., Scott P., Edsjö J., Conrad J., Bergström L., 2010, [Journal of High Energy Physics](#), 2010
- Ashton G., et al., 2022, [Nature Reviews Methods Primers](#), 2
- Buchner J., 2021, UltraNest – a robust, general purpose Bayesian inference engine ([arXiv:2101.09604](#))
- Feroz F., Hobson M. P., Bridges M., 2009, [Monthly Notices of the Royal Astronomical Society](#), 398, 1601
- Feroz F., Cranmer K., Hobson M., de Austri R. R., Trotta R., 2011, [Journal of High Energy Physics](#), 2011
- Gelman A., Meng X.-L., 1998, [Statistical Science](#), 13, 163
- Habek M., 2015, [AIP Conference Proceedings](#), 1641, 121
- Handley W., 2021, [Physical Review D](#), 103
- Handley W., 2023a, Nested sampling: powering next-generation inference and machine learning tools for cosmology, particle physics and beyond, King's College London, https://github.com/williamjameshandley/talks/raw/kcl_2023/will_handley_kcl_2023.pdf
- Handley W., 2023b, The scaling frontier of nested sampling
- Handley W., Lemos P., 2019, [Physical Review D](#), 100
- Handley W. J., Hobson M. P., Lasenby A. N., 2015, [Monthly Notices of the Royal Astronomical Society](#), 453, 4385
- Higson E., Handley W., Hobson M., Lasenby A., 2018, [Monthly Notices of the Royal Astronomical Society](#)
- Higson E., Handley W., Hobson M., Lasenby A., 2019, [Statistics and Computing](#), 29, 891–913
- Petrosyan A., Handley W., 2022, [Physical Sciences Forum](#), 5
- Pártay L. B., Bartók A. P., Csányi G., 2010, Efficient sampling of atomic configurational spaces ([arXiv:0906.3544](#))
- Sivia D. S., Skilling J., 2006, *Data Analysis: A bayesian tutorial* (Oxford Science Publications). Oxford University Press
- Skilling J., 2006, [Bayesian Analysis](#), 1